

See discussions, stats, and author profiles for this publication at: <https://www.researchgate.net/publication/23997016>

# Structure Direction of II–VI Semiconductor Quantum Dot Binary Nanoparticle Superlattices by Tuning Radius Ratio

ARTICLE *in* ACS NANO · JULY 2008

Impact Factor: 12.88 · DOI: 10.1021/nn800129s · Source: PubMed

---

CITATIONS

78

---

READS

20

2 AUTHORS, INCLUDING:



Stephen O'Brien

City College of New York

126 PUBLICATIONS 7,688 CITATIONS

SEE PROFILE

# Structure Direction of II–VI Semiconductor Quantum Dot Binary Nanoparticle Superlattices by Tuning Radius Ratio

Zhuoying Chen and Stephen O'Brien\*

Department of Applied Physics & Applied Mathematics, Columbia University, 200 SW Mudd Building, 500 West 120th Street, New York, New York 10027

Self-assembly is a delightful concept, essentially one in which the complex work of engineering is performed by nature's own intent. In materials chemistry, we generally desire that self-assembly produce recognizable and reproducible structures of order and periodicity, thus demonstrating that components can be placed in predetermined positions (e.g., on a lattice). Such observations are a prelude to the conviction that functional architectures can be purposely designed in this way. Self-assembly of binary colloidal micrometer-sized hard spheres, by sedimentation or slow evaporation of a solvent suspension, has been studied intensively since the early 1980s.<sup>1–12</sup> Recently, the creation of binary particle superlattices by self-assembly was applied to the field of nanoparticles (NPs),<sup>13–24</sup> creating an opportunity to combine nanoparticle components with distinct properties and fine-tune the collective properties of the superlattices.<sup>22,25–28</sup> In the field of superlattices of micrometer-sized hard spheres, unless by carefully adjusting the particle surface charges<sup>5,7–9</sup> or by applying an external field,<sup>4</sup> the self-assembly phenomenon is generally considered to be an entropically driven process,<sup>10,12,29–31</sup> rationalized by the space filling principle.<sup>32,33</sup> By comparison, the formation mechanisms of binary nanoparticle superlattices (BNSLs) still remain unclear. The diversity of the structures synthesized in systems as different as noble metals, semiconductors, and magnetic insulators sustains the idea that these structures result from a subtle equilibrium between various possible driving forces.<sup>18,19,34</sup> The self-assembly of BNSLs from organically stabilized NPs is therefore considered as a

**ABSTRACT** We report a nanoparticle radius ratio dependent study of the formation of binary nanoparticle superlattices (BNSLs) of CdTe and CdSe quantum dots. While keeping all other parameters identical in the system, the effective nanoparticle radius ratio,  $\gamma_{\text{eff}}$ , was tuned to allow the formation of five different BNSL structures,  $\text{AlB}_2$ , *cub*- $\text{NaZn}_{13}$ , *ico*- $\text{NaZn}_{13}$ ,  $\text{CaCu}_5$ , and  $\text{MgZn}_2$ . For each structure,  $\gamma_{\text{eff}}$  is located close to a local maximum of its space-filling factor, based on a model for space filling principles. We demonstrate the ability to select specific BNSLs based solely on  $\gamma_{\text{eff}}$  highlighting the role of entropic forces as a driver for self-assembly.

**KEYWORDS:** nanoparticle · quantum dot · self-assembly · superlattice · entropy driven · crystallization

complex process involving a balance between entropy,<sup>19,21</sup> Coulomb interactions from particle surface charges,<sup>18,19,35</sup> London–van der Waals forces,<sup>19</sup> charge-dipole,<sup>19</sup> dipole–dipole,<sup>19,34</sup> and ligand–ligand interactions.<sup>21,23,24,36–38</sup> This process is further complicated by the fact that the contributions of each of these driving forces varies when the nature of the nanoparticles, their sizes, the nature of substrates, the ligands, the solvents, or the synthetic procedure are changed.

Further progress in the fundamental understanding of BNSL formation requires a systematic investigation of the influence of these parameters independently. A possible methodology is therefore to isolate a parameter which is suspected to play a dominant role in the formation mechanism, and to study the effects of its variation on the resulting structures adopted by the superlattices. Applications of this methodology would be of great help in formulating general principles to explain, at least qualitatively, the trends in the observed structures. And furthermore improve the basis for rational design of BNSLs.

In this paper a series of experiments have been carried out to investigate the influence of the NP radius ratio  $\gamma$  on the ge-

See the accompanying Perspective by Talapin on p 1097.

\*Address correspondence to so188@columbia.edu.

Received for review March 2, 2008 and accepted April 13, 2008.

Published online May 7, 2008.  
10.1021/nn800129s CCC: \$40.75

© 2008 American Chemical Society

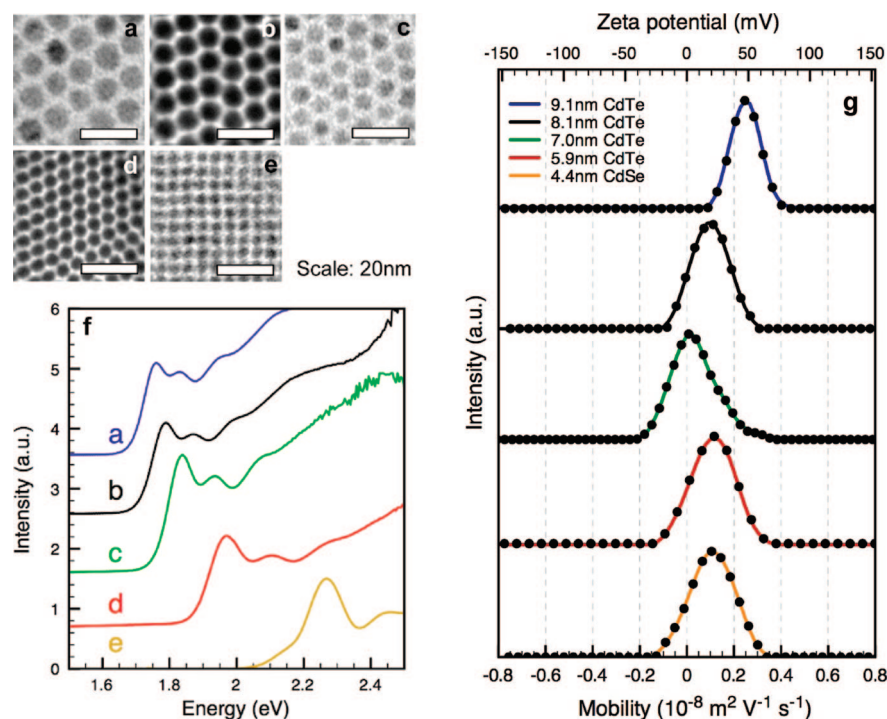


**Figure 1.** Characterization of single component semiconductor nanoparticles: (a–e) TEM images of (a) 9.1 nm CdTe, (b) 8.1 nm CdTe, (c) 7.0 nm CdTe, (d) 5.9 nm CdTe, and (e) 4.4 nm CdSe. All scale bars represent 20 nm. (f) UV–vis absorption spectra of the above nanoparticle solutions in toluene. (g) Electrophoretic mobility and zeta-potential measurements performed separately on the above nanoparticle solutions in chloroform.

ometry of the superlattices obtained by self-assembly of CdTe and CdSe quantum dots. In a previous paper, we demonstrated the formation of cuboctahedral- $\text{AB}_{13}$  (cuboctahedral modification of  $\text{NaZn}_{13}$ ) and  $\text{CaCu}_5$  structures in this system for an effective particle radius ratio  $\gamma_{\text{eff}} \approx 0.62$ .<sup>21</sup> Careful investigation of the driving forces leading to the formation of these structures allowed us to eliminate the likelihood of interparticle Coulomb interactions or London–van der Waals as the major driving forces. We concluded that these structures are more likely to form under a combined influence of surface (mainly ligand–ligand VdW) and entropic (hard sphere packing) effects. The NPs radius ratio therefore emerges as a highly relevant parameter to investigate in such a system, as optimal space fillings are usually obtained for distinct structures when  $\gamma$  is varied. Here we extend our previous work by residing within the same NP system (CdTe–CdSe), exploring a radius ratio from  $\gamma_{\text{eff}} \approx 0.57$  to 0.81, and studying the “engineered” BNSL structures obtained. The change of observed BNSL structures by tuning only this geometrical parameter gives further insight into the mechanisms taking place in this system. It also provides quantitative data useful for both future theoretical studies and practical applications of these “metamaterials”. The strength of dipole–dipole interactions in the formation of colloidal BNSLs was also investigated by extending our experiments from the CdTe–CdSe system into the CdTe–Au system while keeping the radius ratio almost identical.

## RESULTS AND DISCUSSION

### Characterization of Nanoparticle Components to Build

**CdTe–CdSe Binary Nanoparticle Superlattices.** The synthetic methods for both CdTe and CdSe NPs are very similar (see Methods). To adjust the  $\gamma$  ratio from 0.57 to 0.81, the size of the CdSe nanoparticles was kept constant, whereas four batches of nearly monodisperse CdTe NPs with increasing sizes were prepared by varying their growth time. The average diameter and relative standard deviation (RSD) of each batch of these NPs were calculated after measuring the diameters of 100 NPs in a typical transmission electron microscopy (TEM) image from each system. Average diameters of CdTe NPs obtained in this work were 9.1, 8.1, 7.0, and 5.9 nm with a RSD of 5.8%, 4.5%, 4.2%, and 6.1%, respectively (Figure 1, a–d). The CdSe NP diameter was 4.4 nm with a RSD of 5.9% (Figure 1e). Powder XRD spectra show the CdTe NPs synthesized adopt the zinc blende phase (supporting figure S1). For the CdSe NPs, similar as previously reported,<sup>39</sup> the XRD pattern permits no clear determination between the zinc blende or wurtzite phases owing to the small crystal size and the resultant diffraction peak broadening (Supporting Information, Figure S1).

UV–vis absorption measurements were performed on NP toluene solutions for these five batches of NPs (Figure 1f). The energy variation of the absorption edge along the series of CdTe NPs with decreasing sizes is particularly visible and directly related to quantum confinement. The data are consistent with previously published size-dependent absorption measurements of

CdTe and CdSe NPs.<sup>40–42</sup> We were not able to obtain nearly monodisperse CdTe NPs of diameter beyond the range 5.9–9.1 nm *without* changing our synthetic method, such as altering the ligand chemistry which might in turn affect the outcome. In the case of CdSe, NPs of diameter 4.4 nm were selected to build BNSL samples because of the relative ease to detect them by TEM in either single component or BNSL samples.

We preformed electrophoretic mobility measurements separately on these five batches of nanoparticles to investigate whether charges are present on the particles and hence whether Coulomb interactions are likely to influence the formation of BNSLs. The measured electrophoretic mobilities,  $\mu$ , are also presented in terms of the zeta potential  $\zeta$  under the Hückel approximation by the relationship  $\mu = 2\epsilon_r\epsilon_0\zeta/3\eta$ , where  $\epsilon_r$  is the relative dielectric constant of the solvent,  $\epsilon_0$  is the dielectric constant of vacuum, and  $\eta$  is the viscosity of the solvent. Using  $\epsilon_r = 4.8$  and  $\eta = 0.542 \text{ N s m}^{-2}$  for chloroform, a 10 mV zeta  $\zeta$  potential corresponds to a mobility of  $0.05227 \times 10^{-8} \text{ m}^2 \text{ V}^{-1} \text{ s}^{-1}$ . This conversion is used in Figure 1g so the horizontal coordinate can be read as either electrophoretic mobility or  $\zeta$  potential. These measurements, presented in Figure 1g, reveal that these particles hold a *similar* and *slightly positive* net average charge under identical solution environments. These results are consistent with both our previous finding<sup>21</sup> and with the fact that CdTe and CdSe NPs are similar in materials nature and synthetic routes. Since the justification of superlattice formation from Coulomb interactions requires the simultaneous presence of NPs carrying charges of opposite signs, we propose to exclude these interactions as a driving force for the self-assembly of CdTe–CdSe quantum dots. This is further supported by the fact that none of our observed BNSL structures (presented in the following section) appears among the theoretically predicted or experimentally observed structures in systems of oppositely charged particles.<sup>5,7–9</sup> Electrophoretic mobility measurements of certain semiconductor and metallic nanoparticles have previously indicated ionization capability and that the charge can be tuned by the ligands.<sup>18</sup> The origins of the observed charges have been attributed to possible uncompensated internal electric polarizations.<sup>43</sup> Further, the addition of surfactants in nonpolar solvents can form reverse micelles which act as charge carriers.<sup>44</sup> What is currently clear is that ionization of the nanoparticles is highly dependent on their synthetic history and conditions employed for solution control. In this case, we maintained strict conditions for minimization of the influence of any charge during BNSL preparation.

The combinations of the 9.1, 8.1, 7.0 and 5.9 nm diameter CdTe, respectively, with the 4.4 nm CdSe NPs give an effective radius ratio ( $\gamma_{\text{eff}}$ )<sup>17,19</sup>  $\approx 0.57, 0.63, 0.71$ , and 0.81. The effective radius ratio  $\gamma_{\text{eff}}$  is derived from the ratio of small to large *effective particle diameter* ( $d_{\text{eff}}$ ),

which is defined as the diameter of the inorganic core plus twice the thickness of the organic ligand shell.<sup>19</sup> The ligands used in CdTe NP synthesis include octadecylphosphonic acid (ODPA) and trioctylphosphine oxide (TOPO) and in the CdSe NP synthesis include stearic acid, octadecylamine (ODA), and TOPO. The thickness of the organic ligand shell was measured by analyzing the single component nanoparticle FCC packing TEM images. In each system, this thickness was calculated as half of the average interparticle distance along a close-packed direction on the  $[011]_{\text{sl}}$  or  $[111]_{\text{sl}}$  zone axis. From these TEM observations, the thicknesses of the ligand shells of the four different batches of CdTe NPs are similar and on average are  $\sim 0.8$  nm, while in the case of CdSe NPs are at  $\sim 0.85$  nm. These values are consistent with those obtained in similar semiconductor NP systems.<sup>19,21</sup>

**Characterization of Binary Nanoparticle Superlattices.**  $\gamma_{\text{eff}} \approx 0.57$  (by 9.1 nm CdTe and 4.4 nm CdSe). Three types of superlattice structures, cuboctahedral- $\text{AB}_{13}$  (*cub-AB*<sub>13</sub>), icosahedral- $\text{AB}_{13}$  (*ico-AB*<sub>13</sub>) isostructural with  $\text{NaZn}_{13}$ , and  $\text{AB}_2$  isostructural with  $\text{AlB}_2$  were observed in this system on their substrates after slow drying of the binary nanocrystal solution. In this system the *ico-AB*<sub>13</sub>, *cub-AB*<sub>13</sub>, and  $\text{AlB}_2$  structures were found to coexist for all different CdTe/CdSe concentration ratios attempted, although the samples from the 1:13 and 1:16 concentration ratios showed greater preponderance of domains crystallized in the *ico-AB*<sub>13</sub> and *cub-AB*<sub>13</sub> structures while the sample from the 1:3 concentration ratio showed more domains of the  $\text{AlB}_2$  structure. The *cub-AB*<sub>13</sub> structure<sup>2</sup> can be considered as the cuboctahedral modification of  $\text{NaZn}_{13}$  (and thus for simplicity we will call it *cub-NaZn*<sub>13</sub> in this work). It is a cubic lattice with the A particles in the corners of the cube, B<sub>I</sub> particles at the body center of the cube and 12 B<sub>II</sub> particles forming a regular cuboctahedron around B<sub>I</sub>. The *ico-AB*<sub>13</sub> (*ico-NaZn*<sub>13</sub>)<sup>45</sup> structure arises from a distortion of the cuboctahedron into an icosahedron. To pave perfectly the direct space, adjacent icosahedrons have to be twisted by 90° with respect to each other along the three dimensions. The *ico-NaZn*<sub>13</sub> unit cell therefore has to be described by a  $2 \times 2 \times 2$  arrangement of the cubic subcells. These two structures, *cub-NaZn*<sub>13</sub> and *ico-NaZn*<sub>13</sub>, were already found to coexist in other BNSL systems.<sup>17,20</sup> The  $\text{AlB}_2$  structure<sup>46</sup> can be described as a hexagonal lattice where the A particles form a simple hexagonal unit cell with two B particles occupying the trigonal prismatic interstices of the intermediate layer at  $z = 1/2$ . The corresponding three-dimensional crystal structure models are displayed in Figure 2 (m, n, and o). Typical TEM images of these *cub-NaZn*<sub>13</sub>, *ico-NaZn*<sub>13</sub>, and  $\text{AlB}_2$  BNSLs from this system in their  $[001]_{\text{sl}}$  and  $[011]_{\text{sl}}$  zone axis are shown in Figure 2a–f with the model structures projected along the corresponding zone axis in the inset. The lateral dimensions of the *cub-*



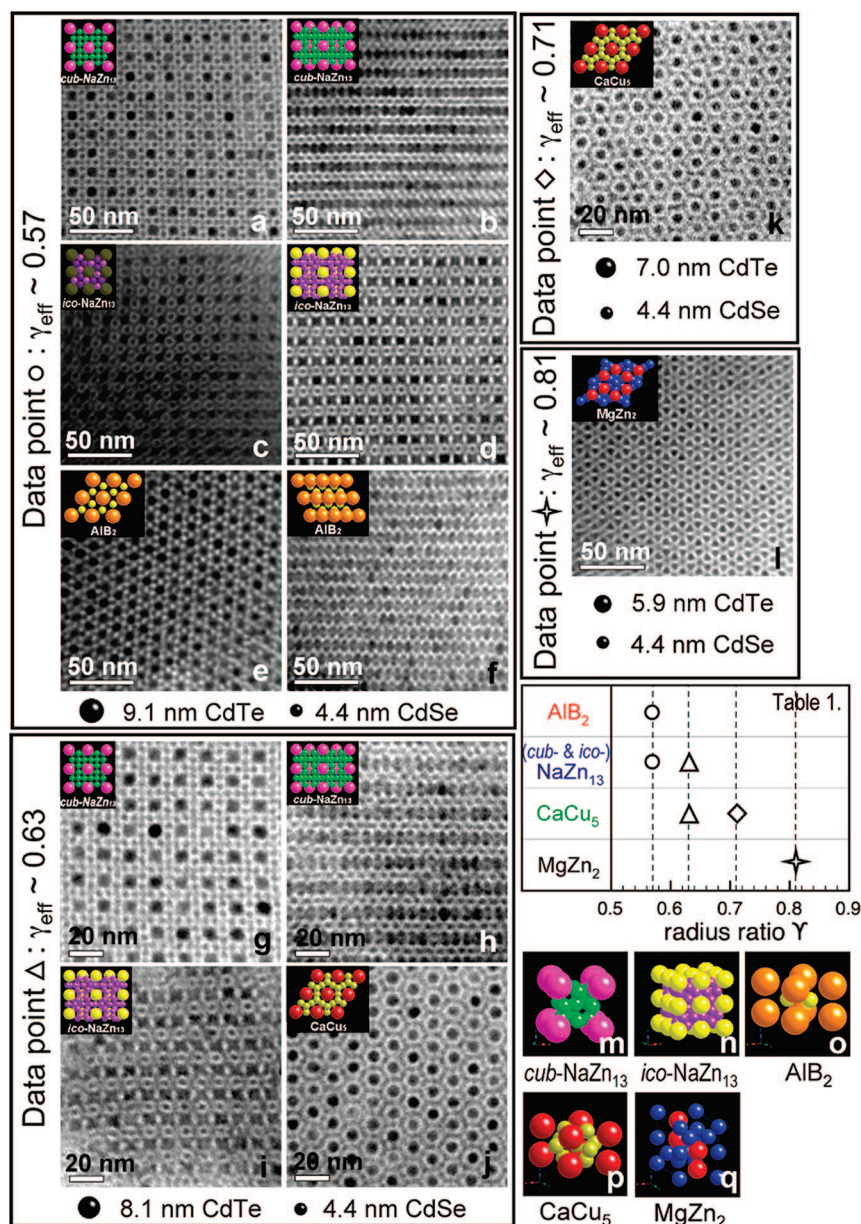


Figure 2. TEM images of binary nanoparticle superlattices self-assembled from (a–f) 9.1 nm CdTe and 4.4 nm CdSe ( $\gamma_{\text{eff}} \approx 0.57$ ), (g–j) 8.1 nm CdTe and 4.4 nm CdSe ( $\gamma_{\text{eff}} \approx 0.63$ ), (k) 7.0 nm CdTe and 4.4 nm CdSe ( $\gamma_{\text{eff}} \approx 0.71$ ), and (l) 5.9 nm CdTe and 4.4 nm CdSe ( $\gamma_{\text{eff}} \approx 0.81$ ) with corresponding modeled structures along the same zone axis. (a, c, e, g, i, k, and l) TEM images along the  $[001]_{\text{sl}}$  zone axis. (b, d, f, h, and j) TEM images along the  $[011]_{\text{sl}}$  zone axis. (m–q) Modeled three-dimensional crystal structure of *cub*-NaZn<sub>13</sub>, *ico*-NaZn<sub>13</sub>, CaCu<sub>5</sub>, AIB<sub>2</sub>, and MgZn<sub>2</sub>, respectively. (Table 1) Summary of all the experimental  $\gamma_{\text{eff}}$  ratios and the observed BNSL structures for each  $\gamma_{\text{eff}}$ .

NaZn<sub>13</sub> and *ico*-NaZn<sub>13</sub> BNSLs can reach  $1\mu\text{m} \times 1\mu\text{m}$ , whereas the AIB<sub>2</sub> BNSLs extend *ca.*  $0.5\mu\text{m} \times 0.5\mu\text{m}$ .

$\gamma_{\text{eff}} \approx 0.63$  (by 8.1 nm CdTe and 4.4 nm CdSe). Three types of superlattice structures, *cub*-NaZn<sub>13</sub>, *ico*-NaZn<sub>13</sub>, and AIB<sub>2</sub> isostructural with CaCu<sub>5</sub>, were observed in this system. The *cub*-NaZn<sub>13</sub> and *ico*-NaZn<sub>13</sub> structures were found on the samples dried from the binary solution containing the CdTe/CdSe concentration ratios of *ca.* 1:13 and 1:16. Samples from the CdTe/CdSe concentration ratio *ca.* 1:6 and 1:9 exhibit a greater preponderance in forming domains of the CaCu<sub>5</sub> structure. The

corresponding modeled three-dimensional crystal structures are displayed in Figure 2 (m, n, and p). The CaCu<sub>5</sub> structure<sup>47</sup> can be described as a simple hexagonal lattice of A particles which are surrounded by a regular arrangement of six B<sub>1</sub> particles occupying the trigonal prismatic interstices of the basal planes. An intermediate layer at  $z = 1/2$  is formed by the B<sub>11</sub> particles only, in a Kagomé-type arrangement. Typical TEM images of these *cub*-NaZn<sub>13</sub>, *ico*-NaZn<sub>13</sub>, and CaCu<sub>5</sub> BNSLs from this system in different zone axis are shown in Figure 2g–j with the corresponding model structures projected along the same zone axis in the inset. The lateral dimensions of the *cub*-NaZn<sub>13</sub> BNSLs are *ca.*  $1\mu\text{m} \times 1\mu\text{m}$ , whereas the *ico*-NaZn<sub>13</sub> and CaCu<sub>5</sub> BNSLs are *ca.*  $0.5\mu\text{m} \times 0.5\mu\text{m}$ .

$\gamma_{\text{eff}} \approx 0.71$  (by 7.0 nm CdTe and 4.4 nm CdSe). The CaCu<sub>5</sub> structure was the only BNSL structure obtained in this system even though experiments with various CdTe: CdSe concentration ratios were attempted. A typical TEM image of these CaCu<sub>5</sub> BNSLs from this system is shown in Figure 2k with the corresponding model structure. These superlattices appear mostly under the form of thin layers (about one to three unit cell heights) and oriented on the  $[001]$  zone axis. The lateral dimensions of these CaCu<sub>5</sub> BNSLs are  $\sim 0.5\mu\text{m} \times 0.5\mu\text{m}$ .

$\gamma_{\text{eff}} \approx 0.81$  (by 5.9 nm CdTe and 4.4 nm CdSe). The AB<sub>2</sub> structure, isostructural with MgZn<sub>2</sub>, is the only BNSL structure obtained for this radius ratio no matter the CdTe/CdSe concentration ratios used. Determined by Friauf<sup>48</sup> in 1927, MgZn<sub>2</sub> (space group  $P6_3/mmc$ ) belongs to the hexagonal Laves phases.<sup>32</sup> The structure of MgZn<sub>2</sub> contains four molecular units per unit cell with the smaller Zn atoms arranged in tetrahedra, joining alternately base-to-base and point-to-point. The larger Mg atoms fit into the “holes” provided by the Zn tetrahedra.<sup>32,49</sup> The three-dimensional crystal structure model is displayed in Figure 2q. A typical TEM image of these MgZn<sub>2</sub> BNSLs from this system in the  $[001]_{\text{sl}}$  zone axis is shown in Figure 2l with the corresponding structure model projected along the same zone axis.

To confirm this assignment, further investigations of the TEM data were undertaken. A large view of a very well-crystallized area of the sample is dis-

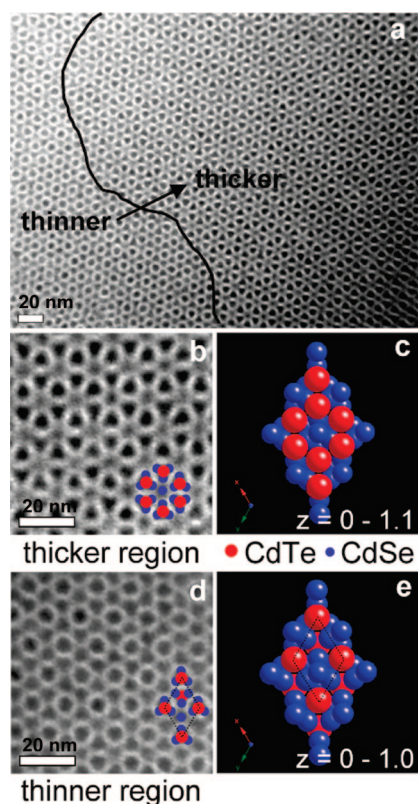


**Figure 3.** TEM images of binary nanoparticle superlattices isostructural with  $\text{MgZn}_2$  in the  $[001]_{\text{SL}}$  zone axis in the system of 5.9 nm CdTe–4.4 nm CdSe: (a) large view TEM image showing two different sample thicknesses; (b,d) details of the nanoparticle arrangements of the thicker and thinner region in panel a, respectively; (c,e) structural model in the  $[001]$  zone axis with  $z = 0 - 1.1$  and  $z = 0 - 1.0$  (one unit cell thickness), respectively.

played in Figure 3a. A sudden change in the experimental contrast is observed when moving from the left to the right-hand side of the picture, the approximate separation between these two zones being symbolized by a black line. As the intensity in a TEM micrograph is, in first approximation, inversely proportional to the absorption and therefore to the thickness of the sample, the brightest (left) part of the picture corresponds to the thinnest part and the darkest (right) part to the thickest part of the superlattice. This variation of the contrast is therefore clearly associated to a thickness variation (not EM defocus). When carefully analyzed, the contrast observed in the thinnest region is in excellent agreement with the structure model of the  $\text{MgZn}_2$  lattice of thickness of one unit cell (Figure 3d,e). When an additional layer of CdTe particles is added, starting a second unit cell, the hexagonal pattern characteristic of the contrast observed in the thickest part of the sample is reproduced (Figure 3b,c). This variation of the experimental contrast therefore provides additional information on the third dimension of the crystal, missing when the superlattices only grow along one particular zone axis, and confirms here the presence of the  $\text{MgZn}_2$  structure.

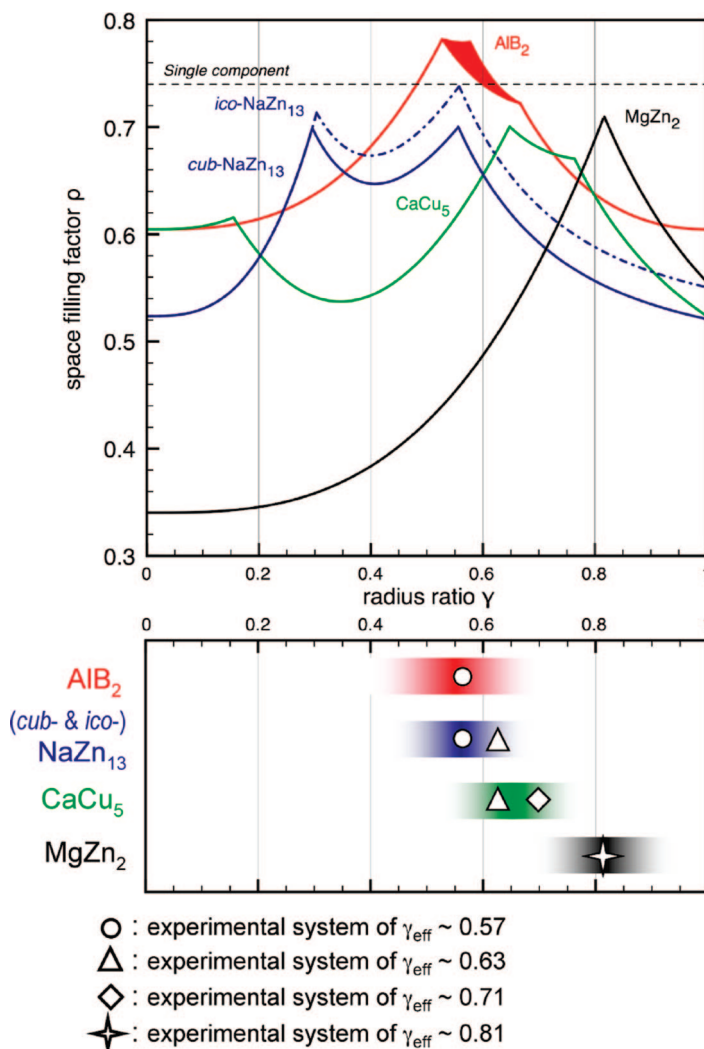


**Figure 4.** Space-filling curves of  $\text{AIB}_2$ ,  $\text{cub-NaZn}_{13}$ ,  $\text{ico-NaZn}_{13}$ ,  $\text{CaCu}_5$ , and  $\text{MgZn}_2$  for the range of radius ratio  $0 \leq \gamma \leq 1$  with data points of  $\gamma_{\text{eff}}$  from each experimental system and the corresponding observed BNSL structures in the CdTe–CdSe binary NP system. Color guides in the range of  $\pm 10\%$  of the local maximum of each space-filling curve are made. The space-filling curves of  $\text{AIB}_2$ ,  $\text{cub-NaZn}_{13}$ , and  $\text{ico-NaZn}_{13}$  are obtained by Murray and Sanders.<sup>2</sup> The space-filling curve of  $\text{MgZn}_2$  is obtained by Parthé.<sup>33</sup> The space-filling curves of  $\text{CaCu}_5$  is obtained by our previous work.<sup>21</sup> The space-filling factor ( $p = 0.7405$ ) corresponding to the single component close-packed structure is indicated by the dotted line.

#### Correlations of the Observed Binary Nanoparticle Superlattice Structures with Space-Filling Factors.

**Entropy driven crystallization.** Entropy driven crystallization can be universally understood by resolving the entropy of the system into configurational entropy and free volume entropy.<sup>29–31,50,51</sup> For hard particles, the potential energy is zero when particles do not overlap and infinite when they interpenetrate. Consider the particles in a system of shrinking volume, such as the case during solvent evaporation. Confining the spheres to an ever shrinking volume (increasing density) forces one of two outcomes: to form a randomly jammed structure, resembling a disordered fluid phase, or to form a crystal lattice structure. The lattice structure decreases the configurational entropy compared with a disordered fluid phase because each particle is required to



order with respect to one another, but in a lattice, each sphere has maximized its own free volume entropy in terms of space to perform local motions of translation (vibration) and rotation. An increase in macroscopic order is driven by an increase in microscopic disorder, and entropy therefore favors crystallization. In the case of hard spheres the packing factor  $\rho = 0.64$  for disordered fluid phase packing is lower than  $\rho = 0.74$  for FCC packing. This implies the entropy of the crystal state is higher than that of the liquid state.<sup>52</sup> In the case of superlattices the system is further complicated by the question as to why the two components do not phase separate into two FCC lattices, one of the large particles and one of the small particles, since this would frequently appear to generate a higher packing factor. From packing diagrams (Figure 4) it is clear that the  $AB_2$  structure can be rationalized by entropy because of the optimization of close packing, since it exceeds  $\rho = 0.74$  for certain radius ratio, however the  $cub-AB_{13}$  structure does not, reaching a maximum close to  $\rho = 0.7$ . A theoretical explanation for the  $AB_{13}$  structure has been proposed with the introduction of an additional factor, ascribed to “entropy of mixing” which serves to adjust the final free energy of the system.<sup>53</sup> Such arguments can be applied to the preferential formation of  $AB_x$  compared to their segregated counterparts. It is here that it serves to recall that the nanoparticles are not hard spheres, but have a layer of ligands and a core. They are therefore capable of interparticle interactions, be they attractive or repulsive, and may favor certain structures dictated by coordination number. We discuss these features where relevant to our experimental observations in subsequent sections.

Using this approach, a binary nanoparticle system is expected to adopt the crystal structure of the form  $AB_x$  that can fill space most efficiently, that is, that maximizes the space-filling factor  $\rho$  for the radius ratio  $\gamma$  characteristic of the system. When considering the space filling curves of the different structures observed experimentally in this work, namely  $AlB_2$ ,  $cub-NaZn_{13}$ ,  $ico-NaZn_{13}$ ,  $CaCu_5$ , and  $MgZn_2$ , we noticed that the BNSL structures systematically form for specific radius ratio values corresponding to a local space-filling factor  $\rho$  maximum (Figure 4). When two structures present a relatively high space-filling factor for the same radius ratio, they are found to coexist in the sample as in the case of  $AlB_2$  and  $NaZn_{13}$  for  $\gamma = 0.57$  or for  $NaZn_{13}$  and  $CaCu_5$  for  $\gamma = 0.63$ . The proportions of these two phases depend essentially on the macroscopic CdTe/CdSe concentration ratio used to make the binary NP solution and the local CdTe/CdSe concentration ratio which can vary in different sample areas.

To illustrate these clear correlations found between the occurrence of a specific crystal structure in the experiments and the location of its local maxima as a function of the radius ratio  $\gamma$ , the space-filling curves for the five structures observed experimentally are repro-

duced from the literature in Figure 4 (top). In the lower part of the figure, we report experimental data corresponding to the observations obtained for four values of the radius ratio in our CdTe–CdSe binary nanoparticle system. Along with the data points, color guides in the range of  $\pm 10\%$  of the local maximum of each space-filling curve are made. The  $AlB_2$  structure represents a particular case in the way of being the only structure to reach higher space-filling factors than the single component close-packed structure for the range  $0.48 \leq \gamma \leq 0.62$ . The space-filling curves of  $AlB_2$ ,  $cub-NaZn_{13}$ ,<sup>82</sup> and  $ico-NaZn_{13}$ <sup>83</sup> are plotted in accordance with Murray and Sanders;<sup>2</sup> the space-filling curve of  $MgZn_2$  is plotted with Parthé.<sup>33</sup> The space-filling curve of  $CaCu_5$  was obtained in our previous work.<sup>21</sup>

To summarize: The different BNSL structures in Figure 2 are formed when the nanoparticle radius ratio is maximized for space filling. This leads to the conclusion that the formation of BNSLs in the CdTe–CdSe nanoparticle system is likely an entropically driven process. This is also supported by the fact that strong interparticle interactions can be safely ruled out. Owing to the relative small solvent-retarded Hamaker constants of these semiconductor materials in hydrocarbon medium,<sup>19,54</sup> we also demonstrated in a previous work that the London–van der Waals interaction of a pair of CdTe–CdSe nanoparticles under a typical interparticle distance is lower or comparable to the thermal energy  $k_B T$  at room temperature.<sup>21</sup> Therefore, a qualitative trend can be drawn from these experiments. Each of the five structures observed in the CdTe–CdSe binary nanoparticle system form only when the radius ratio between the two particles corresponds to the optimal occupation of space offered by this structure. In such a system, where strong pair interactions between particles are absent, entropic effects are therefore still believed to drive the crystallization process.

The observed BNSL structures in this work and the sequence of radius ratio is almost identical to those observed in binary colloidal micrometer-sized particle systems. Yoshimura and Hachisu<sup>10–12</sup> observed superlattices of  $AlB_2$  ( $0.5 \leq \gamma_{eff} \leq 0.56$ ),  $NaZn_{13}$  ( $0.61 \leq \gamma_{eff} \leq 0.63$ ),  $AB_4$  ( $\gamma_{eff} \approx 0.62$ ),  $CaCu_5$  ( $0.72 \leq \gamma_{eff} \leq 0.75$ ), and  $MgCu_2$  ( $0.77 \leq \gamma \leq 0.84$ ) in their work of order formation in binary submicrometer-sized latex particles, which are modeled as hard spheres. The agreement underscores the validity of entropy as a major driving force for the formation of BNSLs of CdSe–CdTe. Further, the occurrences of the same structures at atomic scale, micrometer-scale, and nanoscale suggest entropy as a general and potentially useful driving force in self-organization over a wide range of length scales.

**Effect of Dipole Interactions.** Colloidal II–VI semiconductor quantum dots, of either wurtzite, zincblende, or rock salt structures, have been widely reported to possess a permanent dipole moment.<sup>34,55–60</sup> The nanocrystal dipole moments are currently understood to originate

from the noncentrosymmetric crystal structure (e.g., wurtzite),<sup>55,57</sup> or the distribution of differently terminated polar crystal facets<sup>58</sup> or surfaces with localized charges,<sup>61</sup> if the crystal structure is centrosymmetric. The formation of anisotropic features in single component quantum dot self-assembly, such as various chain-like structures (pearl-necklace structure,<sup>62</sup> nanowires or nanorings,<sup>58</sup> and worm-like structures<sup>59</sup>) or even sheets in solution<sup>60</sup> have been mainly attributed to dipole couplings. Recently dipole–dipole interactions were further suggested to play an important role in the self-organization of organically stabilized single component semiconductor superlattices by presenting calculations for the case of PbS and PbSe nanocrystals.<sup>34</sup>

To test the strength of dipole coupling in the formation of BNSLs, we purposefully extended the CdTe–CdSe system by exchanging one of the semiconductor nanoparticle components by metal nanoparticles, known for not possessing permanent dipole moments. If dipole coupling has an important contribution to the formation of BNSL structures in our CdTe–CdSe system, changing one of the polar constituents by a nonpolar kind should in theory change the BNSL structural outcome. Gold nanoparticles of average diameter 5.5 nm (RSD  $\approx$  6.7%) were synthesized following the Brust's method<sup>63</sup> plus a digestive ripening process<sup>64</sup> (details described in Methods). These gold NPs are capped by 1-dodecanethiol and the thickness of the ligand shell is measured by TEM to be  $\sim$ 0.7 nm (thus  $d_{\text{eff}}$  for Au is  $\sim$ 6.9 nm). Readily dissolved in organic solutions such as toluene or chloroform, these gold NPs in solution display an characteristic UV–vis absorption peak around 530 nm (Supporting Information Figure S2) due to the surface plasmonic effects.<sup>65</sup>

By combining the 8.1 nm batch CdTe and the 7.0 nm CdTe, respectively, with these 5.5 nm Au, we created two CdTe–Au binary systems of  $\gamma_{\text{eff}} \approx 0.71$  and 0.80. Following the identical BNSL preparation procedure used in the CdTe–CdSe system, we obtained CdTe–Au BNSLs isostructural with the  $\text{CaCu}_5$  structure in the system of  $\gamma_{\text{eff}} \approx 0.71$  (Figure 5a) and  $\text{MgZn}_2$  structure in the system of  $\gamma_{\text{eff}} \approx 0.80$  (Figure 5c). TEM images of these CdTe–Au BNSLs also show excellent agreements of the NP arrangements with their model structures (Figure 5b,d). Owing to differences in atomic weights, under TEM the small metal NPs appear darker than the big CdTe NPs, while in the CdTe–CdSe cases the small CdSe NPs generally appear much lighter than the big CdTe NPs. The observed BNSL structures in these CdTe–Au systems show strikingly similar correlations with the space-filling factors of these structures as in the CdTe–CdSe system: These structures form for specific radius ratio values corresponding to a local space-filling factor  $\rho$  maximum.

We conclude that these BNSL structures do not appear to depend on permanent dipole interactions. We conjecture this may be due to the hydrophobic

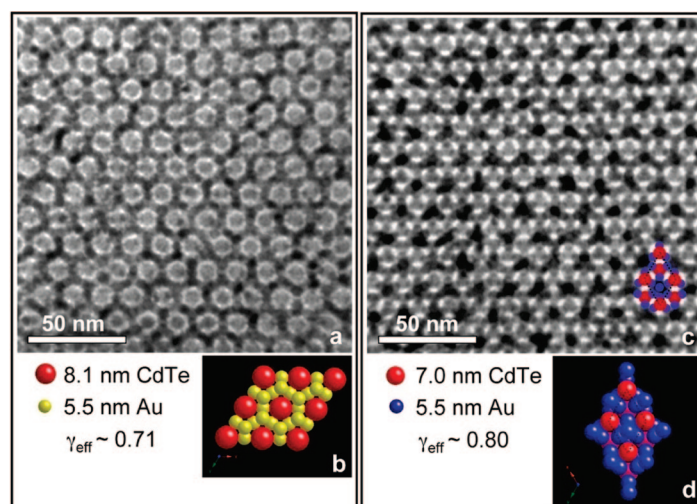


**Figure 5.** TEM images of binary nanoparticle superlattices self-assembled from (a) 8.1 nm CdTe and 5.5 nm Au and (c) 7.0 nm CdTe and 5.5 nm Au (with highlighted NP arrangements). (b and d) corresponding modeled structures of  $\text{CaCu}_5$  and  $\text{MgZn}_2$ , respectively, both projected along the  $[001]_{\text{sl}}$  zone axis.

ligands;<sup>62</sup> one of the key steps in the preparation of nanowires from CdTe quantum dots (due to dipole coupling) was the removal of excess stabilizer. In addition, several of the structures were reported previously in metal–metal BNSL systems.<sup>13,20,66</sup>

**The Role of Coordination.** The observed BNSL structures do not follow the space-filling principle *exactly*. For example, even though the space-filling factor  $\rho$  of the  $\text{MgZn}_2$  structure at  $\gamma \approx 0.82$  reaches a maximum value of 0.71, it is still below the  $\rho$  value of the single component particle close-packed structures (0.74). From the strict point of view of maximization of entropy, it is still better for the binary NPs of this radius ratio to segregate into their own single component close-packed structures than to form the Laves phase. However, experimentally, we did observe structures such as  $\text{MgZn}_2$ ,  $\text{CaCu}_5$ ,  $\text{cub-NaZn}_{13}$ , and  $\text{ico-NaZn}_{13}$  (when  $\gamma$  deviates 0.56) even though their space-filling factors of the specific  $\gamma$  are below 0.74 or even not the highest among all the curves plotted. Theoretical calculations have sought to explain this observation through Helmholtz energy minimization, simulation, and the construction of appropriate phase diagrams.<sup>29,53</sup> In addition to these propositions, we wish to introduce an experimental observation related to a deviation from the rigid hard sphere model,<sup>21</sup> and the role of coordination.

An important similarity found between all the BNSL structures observed in our CdTe–CdSe NP system is that they are highly coordinated structures. For example, the  $\text{MgZn}_2$  structure, having a coordination number (CN) of 12 for the Zn sites and a CN of 16 for the Mg sites, is a Frank–Kasper phase (characterized by the occurrence of layered structures containing exclusively tetrahedral interstices and coordination polyhedra with *only* triangular faces and CN of 12, 14, 15, or 16).<sup>67–69</sup> Among all the structures we observed, except  $\text{AlB}_2$  which represents a special case due to its very high



space-filling factor, all coordination polyhedra found in the rest of the observed structures have  $CN \geq 12$ .<sup>21,70</sup>

The origin of these highly coordinated structures in our BNSL system is attributed to the existence of favorable short-range interactions between particle surface ligands: maximizing coordination number also maximizes ligand–ligand interactions.<sup>21</sup> As suggested by Landman and Luedtke<sup>37</sup> and other previous studies,<sup>38,71–73</sup> ligand–ligand van der Waals interactions in nanoparticles stabilized by hydrophobic alkyl chains (e.g., due to interdigitations of ligand chains, ligand bundling, or chain packing) do effect the final superlattice structure adopted and can stabilize nonclosed-packed structures.

Zilherl and Kamien<sup>36</sup> proposed a contrasting scheme based on their findings in the field of self-assembly of single component micelles of dendritic polymers,<sup>74</sup> where interdigitations of ligands are deemed unfavorable. They proposed that the superstructure formed in such systems should *both* maximize bulk entropy *and* minimize the total contact area between the ligand shells of adjacent particles. By this principle the Frank–Kasper (F–K) structures (including the Lave phases) are proposed to be good candidates with area-minimal regular partitions of space into cells of equal volume (single component case).<sup>36,75</sup> This is supported by the experimentally observed  $A_{15}$  structure (F–K phase,  $\beta$ -tungsten structure) when self-assembling polymer micelles.<sup>74</sup> According to the strict definition of F–K phase<sup>68,69</sup> and the classification by Pearson,<sup>67</sup> among all the structures we observed only the  $MgZn_2$  belongs to the F–K phase. The  $NaZn_{13}$  and  $CaCu_5$  type structures are not F–K phases even though some researchers<sup>76,77</sup> suggested they are highly related to F–K in the way of having coordination polyhedra with large CN and mostly triangular faces. It is still not clear whether Zilherl and Kamien's principle can be used in our BNSL system since (1) the  $A_{15}$  structure is

never observed to our knowledge in experiments involving single component NP self-assembly and (2) the structures of the ligands used in our system<sup>21</sup> are far from dendritic polymers. Further verification of the role of the ligands in determining superlattice structure will require serious theoretical study, involving calculating and comparing the sum of the surface area of the partition cells in each of the structures.

## CONCLUSIONS

In this work, the dependence of superlattice structure on the radius ratio of nanoparticles was studied systematically by self-assembly of CdTe and CdSe quantum dots. Nearly monodisperse CdTe NPs in average diameter of 9.1, 8.1, 7.0 and 5.9 nm and CdSe NPs of 4.4 nm were obtained. The combination of these nanoparticles allowed the exploration of radius ratios in the range  $\gamma_{\text{eff}} \approx 0.57$  to 0.81 while all the other parameters of the system remained exactly the same. Five different BNSL structures,  $AlB_2$ ,  $cub\text{-}NaZn_{13}$ ,  $ico\text{-}NaZn_{13}$ ,  $CaCu_5$ , and  $MgZn_2$  systematically form for specific radius ratio values corresponding to a local maximum in the space-filling factor. To investigate the strength of dipole coupling, we purposefully extended our CdTe–CdSe system by exchanging one of the semiconductor nanoparticle components by metal nanoparticles. For an almost identical  $\gamma_{\text{eff}}$ , we observed the same BNSL structure in the CdTe–Au system as in the CdTe–CdSe system. We conclude that the observed BNSL structures in this work are not specific to the particle species. We demonstrated that in such a system where strong pair interactions between particles are absent, maximization of entropy according to hard-sphere packing principles is the main driver for crystallization. The demonstration of structure direction of superlattices in the binary CdTe–CdSe quantum dot system offers important experimental data for future theoretical studies on BNSLs and their practical applications.

## METHODS

**Characterization Instruments.** TEM characterization was carried out using a JEOL-100 microscope attached with a CCD camera. Powder XRD spectra was obtained using an Inel X-ray diffractometer. UV–vis spectra of nanoparticle solution were taken on a HP 8453 UV/visible spectrophotometer. Electrophoretic mobility measurements were taken on a Malvern Zetasizer Nano-ZS test measurement system.

**Chemicals.** Toluene, ethanol, tetrachloroethylene (TCE), 1-octadecene (ODE), stearic acid (SA), octadecyl phosphonic acid (ODPA), trioctylphosphine oxide (TOPO) (technical grade 90% for CdSe and ReagentPlus 99% for CdTe synthesis), octadecylamine (ODA), CdO, Te, gold chloride, didodecyltrimethylammonium bromide,  $NaBH_4$ , and 1-dodecanethiol were purchased from Aldrich. Trioctylphosphine (TOP) (97%) was purchased from Strem Chemicals. All chemicals were used as received.

**Synthesis of Single Component Semiconductor NPs.** The CdTe NPs synthesis is based on Peng's<sup>78</sup> and Manna's<sup>79</sup> methods and the CdSe synthesis is based on Li's<sup>80</sup> and Kim's<sup>81</sup> methods with minor modifications. In both cases CdO was used as the cadmium

source to prepare the Cd precursor. NP nucleation was triggered by the rapid hot injection of TOP–Te or TOP–Se into the Cd precursor in the presence of a mixture of surfactants. NP diameter was controlled by the injection temperature and the growth time. To narrow size distributions, careful postsynthesis size selection processes were performed by the addition of non-solvent and centrifugation (see Supporting Information for all detailed synthesis steps).

**Synthesis of Gold NPs.** Gold nanoparticles of average diameter 5.5 nm were synthesized following the Brust's method<sup>63</sup> plus a digestive ripening process<sup>64</sup> (see Supporting Information for detailed steps).

**Preparation of Binary Superlattices.** Binary nanoparticle superlattices (BNSLs) were prepared by modifying the methods developed by Redl *et al.*<sup>15</sup> and Shevchenko *et al.*<sup>19</sup> During the last purification (centrifugation and precipitation) procedure of the nanoparticles, the precipitate was dried under vacuum and weighted to determine how much solution is needed to redisperse the nanoparticle precipitate into solution ready for the preparation of BNSLs. Typically, the concentration of each single component CdTe and CdSe particles in solution was controlled

to ca.  $2.7 \times 10^{14}$ /mL (for CdTe) and ca.  $16.8 \times 10^{14}$ /mL (for CdSe), respectively. For both systems we used TCE (with 0.006 volume fraction additive of 1-dodecanethiol) as the solution to disperse the precipitate after the final wash. We found that adding a small amount (0.006 volume fraction) of 1-dodecanethiol into the TCE solution can enhance the formation of BNSLs in the present case. For each pair of CdTe–CdSe binary NPs of a specific particle radius ratio, five bottles of binary nanoparticle solution were made by mixing the CdTe and CdSe single component solutions according to the different CdTe/CdSe concentration ratios of ca. 1:3, 1:6, 1:9, 1:13, and 1:16. Substrates (TEM Cu grids back with amorphous carbon film) were placed in five glass tubes containing 40  $\mu$ L of binary nanoparticle solution corresponding to these concentration ratios. These glass tubes were placed in a stand so that they are tilted by 60–70°. These binary solutions on substrates were first allowed to dry under ambient at room temperature for overnight (~15 h) so that the solutions became highly concentrated but not yet totally dried on the substrates. Then these solutions were further dried for 24 h by placing these tubes on a hot stage (~55 °C) under nitrogen protection at ambient pressure. The preparation procedure of CdTe–Au BNSLs is the same as that for CdTe–CdSe described above.

**Acknowledgment.** S. O'Brien is grateful for support for this project from CAREER Award No. DMR-0348938. This work was also supported in part by the MRSEC program of the National Science Foundation under Award No. DMR-02113574 and by the DoE (DE-FG02-03ER15463). We relied on equipments supported by the NSEC program of the National Science Foundation under Award No. CHE-0117752. We thank G. Radtke (CNRS, Université Paul Cézanne-Aix Marseille III) for useful discussions and comments on the manuscript.

**Supporting Information Available:** Information of detailed synthesis procedure and powder XRD characterization of CdTe and CdSe nanoparticles, and the synthesis procedure and UV–vis absorption data of Au nanoparticles. This material is available free of charge via the Internet at <http://pubs.acs.org>.

## REFERENCES AND NOTES

- Hachisu, S.; Yoshimura, S. Optical Demonstration of Crystalline Superstructures in Binary-Mixtures of Latex Globules. *Nature* **1980**, *283*, 188–189.
- Murray, M. J.; Sanders, J. V. Close-Packed Structures of Spheres of 2 Different Sizes 2. The Packing Densities of Likely Arrangements. *Philos. Mag. A* **1980**, *42*, 721–740.
- Sanders, J. V. Close-Packed Structures of Spheres of 2 Different Sizes 1. Observations on Natural Opal. *Philos. Mag. A* **1980**, *42*, 705–720.
- Yethiraj, A.; Thijssen, J. H. J.; Wouterse, A.; van Blaaderen, A. Large-Area Electric-Field-Induced Colloidal Single Crystals for Photonic Applications. *Adv. Mater.* **2004**, *16*, 596–600.
- Bartlett, P.; Campbell, A. I. Three-Dimensional Binary Superlattices of Oppositely Charged Colloids. *Phys. Rev. Lett.* **2005**, *95*, 128302.
- Cho, Y. S.; Yi, G. R.; Lim, J. M.; Kim, S. H.; Manoharan, V. N.; Pine, D. J.; Yang, S. M. Self-Organization of Bidisperse Colloids in Water Droplets. *J. Am. Chem. Soc.* **2005**, *127*, 15968–15975.
- Leunissen, M. E.; Christova, C. G.; Hynninen, A. P.; Royall, C. P.; Campbell, A. I.; Imhof, A.; Dijkstra, M.; van Roij, R.; van Blaaderen, A. Ionic Colloidal Crystals of Oppositely Charged Particles. *Nature* **2005**, *437*, 235–240.
- Hynninen, A. P.; Christova, C. G.; van Roij, R.; van Blaaderen, A.; Dijkstra, M. Prediction and Observation of Crystal Structures of Oppositely Charged Colloids. *Phys. Rev. Lett.* **2006**, *96*, 165901.
- Hynninen, A. P.; Leunissen, M. E.; van Blaaderen, A.; Dijkstra, M. CuAu Structure in the Restricted Primitive Model and Oppositely Charged Colloids. *Phys. Rev. Lett.* **2006**, *96*, 018303.
- Hachisu, S.; Yoshimura, S. Order Formation in Binary Colloids (Colloid Alloys in Binary Latexes). In *Physics of Complex and Supramolecular Fluids (An Exxon Monograph)*; Safran, S. A., Clark, N. A., Eds.; John Wiley & Sons, Inc.: 1987; pp 221–240.
- Yoshimura, S.; Hachisu, S. Order Formation in Binary-Mixtures of Monodisperse Lattices 0.1. Observation of Ordered Structures. *Prog. Colloid Polym. Sci.* **1983**, *68*, 59–70.
- Yoshimura, S.; Hachisu, S. Order Formation in Binary-Mixtures of Monodisperse Latexes. *J. Phys.* **1985**, *46*, 115–126.
- Kiely, C. J.; Fink, J.; Brust, M.; Bethell, D.; Schiffrin, D. J. Spontaneous Ordering of Bimodal Ensembles of Nanoscopic Gold Clusters. *Nature* **1998**, *396*, 444–446.
- Kiely, C. J.; Fink, J.; Zheng, J. G.; Brust, M.; Bethell, D.; Schiffrin, D. J. Ordered Colloidal Nanoalloys. *Adv. Mater.* **2000**, *12*, 640–643.
- Redl, F. X.; Cho, K. S.; Murray, C. B.; O'Brien, S. Three-Dimensional Binary Superlattices of Magnetic Nanocrystals and Semiconductor Quantum Dots. *Nature* **2003**, *423*, 968–971.
- Saunders, A. E.; Korgel, B. A. Observation of an AB Phase in Bidisperse Nanocrystal Superlattices. *Chemphyschem* **2005**, *6*, 61–65.
- Shevchenko, E. V.; Talapin, D. V.; O'Brien, S.; Murray, C. B. Polymorphism in AB<sub>13</sub> Nanoparticle Superlattices: An Example of Semiconductor-Metal Metamaterials. *J. Am. Chem. Soc.* **2005**, *127*, 8741–8747.
- Shevchenko, E. V.; Talapin, D. V.; Kotov, N. A.; O'Brien, S.; Murray, C. B. Structural Diversity in Binary Nanoparticle Superlattices. *Nature* **2006**, *439*, 55–59.
- Shevchenko, E. V.; Talapin, D. V.; Murray, C. B.; O'Brien, S. Structural Characterization of Self-Assembled Multifunctional Binary Nanoparticle Superlattices. *J. Am. Chem. Soc.* **2006**, *128*, 3620–3637.
- Sra, A. K.; Ewers, T. D.; Xu, Q.; Zandbergen, H.; Schaak, R. E. One-Pot Synthesis of Bi-Disperse FePt Nanoparticles and Size-Selective Self-Assembly into AB<sub>2</sub>, AB<sub>3</sub>, and AB<sub>13</sub> Superlattices. *Chem. Commun.* **2006**, 750–752.
- Chen, Z.; Moore, J.; Radtke, G.; Siringhaus, H.; O'Brien, S. Binary Nanoparticle Superlattices in the Semiconductor-Semiconductor System: CdTe and CdSe. *J. Am. Chem. Soc.* **2007**, *129*, 15702–15709.
- Urban, J. J.; Talapin, D. V.; Shevchenko, E. V.; Kagan, C. R.; Murray, C. B. Synergism in Binary Nanocrystal Superlattices Leads to Enhanced P-Type Conductivity in Self-Assembled PbTe/Ag<sub>2</sub>Te Thin Films. *Nat. Mater.* **2007**, *6*, 115–121.
- Nykypanchuk, D.; Maye, M. M.; van der Lelie, D.; Gang, O. DNA-Guided Crystallization of Colloidal Nanoparticles. *Nature* **2008**, *451*, 549–552.
- Park, S. Y.; Lytton-Jean, A. K. R.; Lee, B.; Weigand, S.; Schatz, G. C.; Mirkin, C. A. DNA-Programmable Nanoparticle Crystallization. *Nature* **2008**, *451*, 553–556.
- Kagan, C. R.; Murray, C. B.; Bawendi, M. G. Long-range Resonance Transfer of Electronic Excitations in Close-Packed CdSe Quantum-dot Solids. *Phys. Rev. B* **1996**, *54*, 8633–8643.
- Zeng, H.; Li, J.; Liu, J. P.; Wang, Z. L.; Sun, S. H. Exchange-Coupled Nanocomposite Magnets by Nanoparticle Self-Assembly. *Nature* **2002**, *420*, 395–398.
- Courty, A.; Mermet, A.; Albouy, P. A.; Duval, E.; Pileni, M. P. Vibrational Coherence of Self-Organized Silver Nanocrystals in F.C.C. Supra-Crystals. *Nat. Mater.* **2005**, *4*, 395–398.
- Lisiecki, I.; Parker, D.; Salzemann, C.; Pileni, M. P. Face-centered Cubic Supra-crystals and Disordered Three-Dimensional Assemblies of 7.5 nm Cobalt Nanocrystals: Influence of the Mesoscopic Ordering on the Magnetic Properties. *Chem. Mater.* **2007**, *19*, 4030–4036.
- Eldridge, M. D.; Madden, P. A.; Frenkel, D. Entropy-Driven Formation of a Superlattice in a Hard-Sphere Binary Mixture. *Nature* **1993**, *365*, 35–37.
- Cottin, X.; Monson, P. A. Substitutionally Ordered Solid-Solutions of Hard-Spheres. *J. Chem. Phys.* **1995**, *102*, 3354–3360.

31. Trizac, E.; Eldridge, M. D.; Madden, P. A. Stability of the AB Crystal for Asymmetric Binary Hard Sphere Mixtures. *Mol. Phys.* **1997**, *90*, 675–678.
32. Laves, F., Crystal Structure and Atomic Size. In *Theory of Alloy Phases*; The American Society of Metals: Cleveland, OH, 1956; pp 124–198.
33. Parthé, E. Space Filling of Crystal Structures. A Contribution to the Graphical Presentation of Geometrical Relationships in Simple Crystal Structures. *Z. Kristallogr.* **1961**, *115*, 52–79.
34. Talapin, D. V.; Shevchenko, E. V.; Murray, C. B.; Titov, A. V.; Kral, P. Dipole-Dipole Interactions in Nanoparticle Superlattices. *Nano Lett.* **2007**, *7*, 1213–1219.
35. Kalsin, A. M.; Fialkowski, M.; Paszewski, M.; Smoukov, S. K.; Bishop, K. J. M.; Grzybowski, B. A. Electrostatic Self-assembly of Binary Nanoparticle Crystals with a Diamond-Like Lattice. *Science* **2006**, *312*, 420–424.
36. Zihler, P.; Kamien, R. D. Maximizing Entropy by Minimizing Area: Towards a New Principle of Self-Organization. *J. Phys. Chem. B* **2001**, *105*, 10147–10158.
37. Landman, U.; Luedtke, W. D. Small is Different: Energetic, Structural, Thermal, and Mechanical Properties of Passivated Nanocluster Assemblies. *Faraday Discuss.* **2004**, *125*, 1–22.
38. Mueggenburg, K. E.; Lin, X.-M.; Goldsmith, R. H.; Jaeger, H. M. Elastic Membranes of Close-Packed Nanoparticle Arrays. *Nat. Mater.* **2007**, *6*, 656–660.
39. Talapin, D. V.; Rogach, A. L.; Mekis, I.; Haubold, S.; Kornowski, A.; Haase, M.; Weller, H. Synthesis and Surface Modification of Amino-Stabilized CdSe, CdTe, and InP Nanocrystals. *Colloids Surf., A* **2002**, *202*, 145–154.
40. Murray, C. B.; Kagan, C. R.; Bawendi, M. G. Synthesis and Characterization of Monodisperse Nanocrystals and Close-Packed Nanocrystal Assemblies. *Annu. Rev. Mater. Sci.* **2000**, *30*, 545–610.
41. Talapin, D. V.; Haubold, S.; Rogach, A. L.; Kornowski, A.; Haase, M.; Weller, H. A Novel Organometallic Synthesis of Highly Luminescent CdTe Nanocrystals. *J. Phys. Chem. B* **2001**, *105*, 2260–2263.
42. Yu, W. W.; Wang, Y. A.; Peng, X. G. Formation and Stability of Size-, Shape-, and Structure-Controlled CdTe Nanocrystals: Ligand Effects on Monomers and Nanocrystals. *Chem. Mater.* **2003**, *15*, 4300–4308.
43. Krishnan, R.; Hahn, M. A.; Yu, Z. H.; Silcox, J.; Fauchet, P. M.; Krauss, T. D. Polarization Surface-Charge Density of Single Semiconductor Quantum Rods. *Phys. Rev. Lett.* **2004**, *92*, 216803.
44. Hsu, M. F.; Dufresne, E. R.; Weitz, D. A. Charge Stabilization in Nonpolar Solvents. *Langmuir* **2005**, *21*, 4881–4887.
45. Shoemaker, D. P.; Marsh, R. E.; Ewing, F. J.; Pauling, L. Interatomic Distances and Atomic Valences in NaZn<sub>13</sub>. *Acta Crystallogr.* **1952**, *5*, 637–644.
46. Pearson, W. B., In *The Crystal Chemistry and Physics of Metals and Alloys*; Pearson, W. B., Ed.; Wiley–Interscience: New York, 1972; pp 494–503.
47. Haucke, W. Crystalline Structure of CaZn<sub>5</sub> and CaCu<sub>5</sub>. *Z. Anorg. Allg. Chem.* **1940**, *244*, 17–22.
48. Friauf, J. B. The Crystal Structure of Magnesium Di-Zincide. *Phys. Rev.* **1927**, *29*, 0034–0040.
49. Pearson, W. B., In *The Crystal Chemistry and Physics of Metals and Alloys*; Pearson, W. B., Ed.; Wiley–Interscience: New York, 1972; pp 657–660.
50. Hunt, N.; Jardine, R.; Bartlett, P. Superlattice Formation in Mixtures of Hard-Sphere Colloids. *Phys. Rev. E* **2000**, *62*, 900–913.
51. Frenkel, D. Order Through Disorder: Entropy Strikes Back. *Phys. World* **1993**, *6*, 24–25.
52. Chaikin, P. M.; Donev, A.; Man, W.; Stillinger, F. H.; Torquato, S. Some Observations on the Random Packing of Hard Ellipsoids. *Ind. Eng. Chem. Res.* **2006**, *45*, 6960–6965.
53. Xu, H.; Baus, M. A Density Functional Study of Superlattice Formation in Hard Sphere Mixtures. *J. Phys. Condens. Matter* **1992**, *4*, L663–L668.
54. Striolo, A.; Ward, J.; Prausnitz, J. M.; Parak, W. J.; Zanchet, D.; Gerion, D.; Milliron, D.; Alivisatos, A. P. Molecular Weight, Osmotic Second Virial Coefficient, and Extinction Coefficient of Colloidal CdSe Nanocrystals. *J. Phys. Chem. B* **2002**, *106*, 5500–5505.
55. Blanton, S. A.; Leheny, R. L.; Hines, M. A.; Guyot-Sionnest, P. Dielectric Dispersion Measurements of CdSe Nanocrystal Colloids: Observation of a Permanent Dipole Moment. *Phys. Rev. Lett.* **1997**, *79*, 865–868.
56. Shim, M.; Guyot-Sionnest, P. Permanent Dipole Moment and Charges in Colloidal Semiconductor Quantum Dots. *J. Chem. Phys.* **1999**, *111*, 6955–6964.
57. Li, L. S.; Alivisatos, A. P. Origin and Scaling of the Permanent Dipole Moment in CdSe Nanorods. *Phys. Rev. Lett.* **2003**, *90*.
58. Cho, K. S.; Talapin, D. V.; Gaschler, W.; Murray, C. B. Designing PbSe Nanowires and Nanorings Through Oriented Attachment of Nanoparticles. *J. Am. Chem. Soc.* **2005**, *127*, 7140–7147.
59. Klokkenburg, M.; Houtepen, A. J.; Koole, R.; de Folter, J. W. J.; Erne, B. H.; van Faassen, E.; Vanmaekelbergh, D. Dipolar Structures in Colloidal Dispersions of PbSe and CdSe Quantum Dots. *Nano Lett.* **2007**, *7*, 2931–2936.
60. Zhang, Z. L.; Tang, Z. Y.; Kotov, N. A.; Glotzer, S. C. Simulations and Analysis of Self-Assembly of CdTe Nanoparticles into Wires and Sheets. *Nano Lett.* **2007**, *7*, 1670–1675.
61. Shim, M.; Guyot-Sionnest, P. Permanent dipole moment and charges in colloidal semiconductor quantum dots. *J. Chem. Phys.* **1999**, *111* (15), 6955–6964.
62. Tang, Z. Y.; Kotov, N. A.; Giersig, M. Spontaneous Organization of Single CdTe Nanoparticles into Luminescent Nanowires. *Science* **2002**, *297*, 237–240.
63. Brust, M.; Walker, M.; Bethell, D.; Schiffrin, D. J.; Whyman, R. Synthesis of Thiol-Derivatized Gold Nanoparticles in a Two-Phase Liquid-Liquid System. *J. Chem. Soc. Chem. Commun.* **1994**, 801–802.
64. Stoeva, S.; Klabunde, K. J.; Sorensen, C. M.; Dragieva, I. Gram-Scale Synthesis of Monodisperse Gold Colloids by the Solvated Metal Atom Dispersion Method and Digestive Ripening and Their Organization into Two- and Three-Dimensional Structures. *J. Am. Chem. Soc.* **2002**, *124*, 2305–2311.
65. Liz-Marzan, L. M. Tailoring Surface Plasmons Through the Morphology and Assembly of Metal Nanoparticles. *Langmuir* **2006**, *22*, 32–41.
66. Shevchenko, E. V.; Talapin, D. V.; Rogach, A. L.; Kornowski, A.; Haase, M.; Weller, H. Colloidal Synthesis and Self-Assembly of CoPt<sub>3</sub> Nanocrystals. *J. Am. Chem. Soc.* **2002**, *124*, 11480–11485.
67. Pearson, W. B., In *The Crystal Chemistry and Physics of Metals and Alloys*; Pearson, W. B., Ed.; Wiley–Interscience: New York, 1972; pp 31–36.
68. Frank, F. C.; Kasper, J. S. Complex Alloy Structures Regarded as Sphere Packings 0.1. Definitions and Basic Principles. *Acta Crystallogr.* **1958**, *11*, 184–190.
69. Frank, F. C.; Kasper, J. S. Complex Alloy Structures Regarded as Sphere Packing 0.2. Analysis and Classification of Representative Structures. *Acta Crystallogr.* **1959**, *12*, 483–499.
70. Pearson, W. B., In *The Crystal Chemistry and Physics of Metals and Alloys*; Pearson, W. B., Ed.; Wiley–Interscience: New York, 1972; pp 754–756; 643–645; 657–659.
71. Badia, A.; Gao, W.; Singh, S.; Demers, L.; Cuccia, L.; Reven, L. Structure and Chain Dynamics of Alkanethiol-Capped Gold Colloids. *Langmuir* **1996**, *12*, 1262–1269.
72. Badia, A.; Singh, S.; Demers, L.; Caccia, L.; Brown, G. R.; Lennox, R. B. Self-Assembled Monolayers on Gold Nanoparticles. *Chem. Eur. J.* **1996**, *2*, 359–363.
73. Zhang, H.; Edwards, E. W.; Wang, D.; Mohwald, H. Directing the Self-Assembly of Nanocrystals Beyond Colloidal Crystallization. *Phys. Chem. Chem. Phys.* **2006**, *8*, 22237.
74. Balagurusamy, V. S. K.; Ungar, G.; Perccec, V.; Johansson, G. Rational Design of The First Spherical Supramolecular Dendrimers Self-Organized in a Novel Thermotropic Cubic



- Liquid-crystalline Phase and The Determination of Their Shape by X-ray analysis. *J. Am. Chem. Soc.* **1997**, *119*, 1539–1555.
75. Rivier, N. Kelvins Conjecture on Minimal Froths and the Counterexample of Weaire and Phelan. *Philos. Mag. Lett.* **1994**, *69*, 297–303.
  76. Hafner, J. Theory of the Formation of Metallic Glasses. *Phys. Rev. B* **1980**, *21*, 406–426.
  77. Hafner, J.; Tegze, M. Structural and Electronic Properties of Crystalline and Glassy Calcium-Zinc Compounds. I. Trigonal Prismatic Ordering or Tetrahedral Close Packing. *J. Phys.: Condens. Matter* **1989**, *1*, 8277–8291.
  78. Peng, Z. A.; Peng, X. G. Formation of High-Quality CdTe, CdSe, and CdS Nanocrystals Using CdO as Precursor. *J. Am. Chem. Soc.* **2001**, *123*, 183–184.
  79. Manna, L.; Milliron, D. J.; Meisel, A.; Scher, E. C.; Alivisatos, A. P. Controlled Growth of Tetrapod-Branched Inorganic Nanocrystals. *Nat. Mater.* **2003**, *2*, 382–385.
  80. Li, J. J.; Wang, Y. A.; Guo, W. Z.; Keay, J. C.; Mishima, T. D.; Johnson, M. B.; Peng, X. G. Large-Scale Synthesis of Nearly Monodisperse CdSe/CdS Core/Shell Nanocrystals Using Air-Stable Reagents via Successive Ion Layer Adsorption and Reaction. *J. Am. Chem. Soc.* **2003**, *125*, 12567–12575.
  81. Kim, J. I.; Lee, J. K. Sub-kilogram-Scale One-Pot Synthesis of Highly Luminescent and Monodisperse Core/Shell Quantum Dots by the Successive Injection of Precursors. *Adv. Funct. Mater.* **2006**, *16*, 2077–2082.
  82. In ref 2 equation 20 should be read  $\rho = \pi(1 + 13\gamma^3)/[6\gamma^3(1 + \sqrt{2})^3]$ .
  83. In ref 2 equation 15 should be read  $\rho = \pi(1 + 13\gamma^3)/6$ .